Synoptic Structure and Evolution of a Kona Low*

IAN MORRISON AND STEVEN BUSINGER

University of Hawaii at Manoa, Honolulu, Hawaii

(Manuscript received 24 February 2000, in final form 30 June 2000)

ABSTRACT

A subtropical cyclone or kona low affected the island of Hawaii on 24–28 February 1997 and brought with it record winds at Hilo, large hail, blizzard conditions at higher elevations, and high surf. Damage estimates for the storm due to crop loss, property damage, and utility line destruction exceed $4 million. A detailed case study of the storm was conducted using all available operational data and data from the National Centers for Environmental Prediction–National Center for Atmospheric Research reanalysis dataset. The kona low formed on 23 February 1997 along a stalled trough northeast of the Hawaiian Islands and is investigated during five evolutionary stages: (i) incipient, (ii) intensifying, (iii) mature, (iv) weakening, and (v) dissipating.

The system's initial development is linked to dynamics at the 250-mb level. The maximum circulation, absolute vorticity, divergence, and height anomalies all occurred at 250 mb during the period of most rapid deepening. Cold anomalies occurred in a deep layer between 850 and 250 mb that tilted eastward with height. Quasigeostrophic analysis showed enhanced vorticity to the west of a thickness trough, a configuration that maintained an area of positive vorticity advection to the west of the surface low and over new convection east and southeast of the low. The vorticity tendency is dominated by the advection of vorticity aloft in this case, especially during the incipient and intensifying stages. The vorticity tendency is dominated by the generation of vorticity by divergence in the lower troposphere.

Cloud bands with embedded convective cells formed on the low's eastern side and propagated eastward, eventually leaving the area of synoptic-scale ascent and losing their convective properties. Areas where the best-lifted index values were less than zero and areas of positive low-level advection of equivalent potential temperature coincided with regions of deep convection, as inferred from satellite imagery.

1. Introduction

Kona lows are subtropical cyclones[1] that occur during the cool season in the north-central Pacific. The Hawaiian word, *kona*, meaning leeward, is used to describe winds with a southerly component that replace the usually persistent trade wind regime. Historically kona lows have produced a variety of weather-related hazards including heavy rains, hailstorms, flash floods, landslides, high winds, large surf and swell, waterspouts, and severe thunderstorms (Schroeder 1977a,b; Ramage 1995; Kodama and Barnes 1997; Businger et al. 1998).

A strong kona low affected the Hawaiian Islands from 24 to 28 February 1997 (Fig. 1). The island of Hawaii (Big Island) experienced high winds and winter storm conditions on the summits of Mauna Kea and Mauna Loa, and large surf (6 m) buffeted all islands. As the low approached and passed the Big Island from east to west, record northerly winds (26 m s^{-1} gusts) in Hilo gradually weakened and turned to the east and then south. The southerly winds brought thunderstorms, uncommonly large hail (13-mm diameter), and heavy rain to the Big Island and Maui on 27 and 28 February. The Hilo pressure trace recorded a lowest pressure of 1006 mb on 26 February with strong winds prior to this time. Orographic enhancement by Mauna Kea caused acceleration of the northerly flow on the eastern slope of the volcano, which likely contributed to the record winds in Hilo (see inset, Fig. 1a). The largest daily rainfall occurred after the low passed to the west of the Big Island. Damage estimates due to crop loss, property damage, and utility line destruction exceeded $4 million (NCDC 1997).

Simpson (1952) was the first to describe kona lows, referring to the systems as kona cyclones. Simpson's work used standard observations and rawinsonde soundings available for two kona lows and Northern Hemi-

* School of Ocean and Earth Science and Technology Contribution Number 5305.

Corresponding author address: Steven Businger, Department of Meteorology, University of Hawaii at Manoa, 2525 Correa Rd., Honolulu, HI 96822.
E-mail: businger@soest.hawaii.edu

[1] Subtropical cyclones, as the term is used here, are cold-core systems with some tropical cyclone characteristics that occur in subtropical latitudes (e.g., Hebert and Poteat 1975).

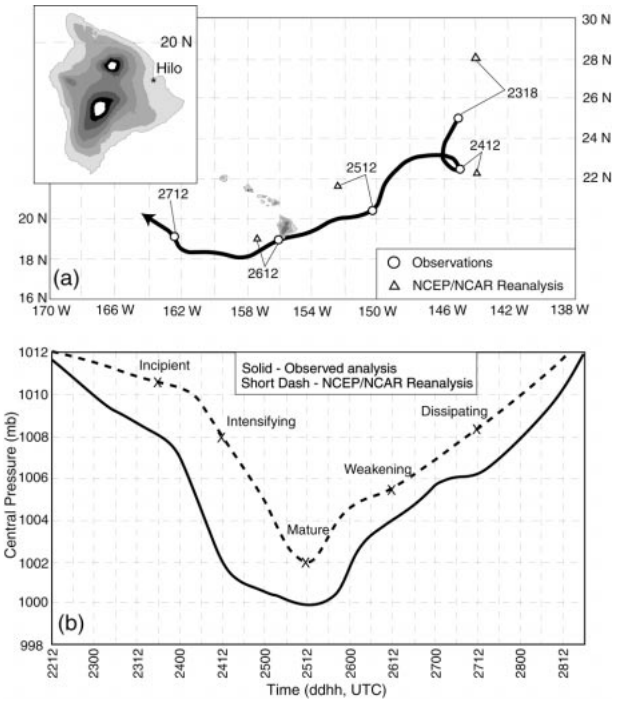

FIG. 1. (a) Comparison of storm track (dark line) for the subjective analysis (circles) and NCEP–NCAR reanalysis (triangles). Each stage is labeled with the first two numbers indicating the day and the last two numbers indicating the hour in UTC time. The inset shows the island of Hawaii with terrain shading every 500 m. (b) Pressure traces for the subjective analysis and the NCEP–NCAR reanalysis. Each stage is labeled and marked on the reanalysis trace.

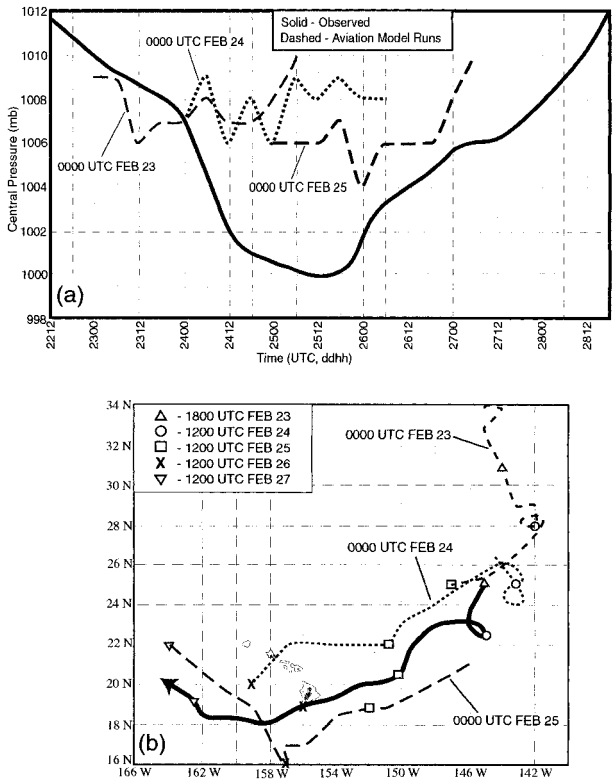

FIG. 2. (a) Pressure traces from the subjective analysis (solid line) and aviation model forecasts (dashed lines labeled with time of run) from 0000 UTC on 23, 24, and 25 Feb 1997. (b) Storm track from the subjective analysis (solid line) and aviation model forecasts (dashed lines, labeled with time of run) from 0000 UTC on 23, 24, and 25 Feb 1997. The forecast duration is 60 h.

sphere weather maps to analyze 76 previous kona lows that occurred in the Pacific over a 20-yr period. Simpson inferred that kona lows are cold core with their strongest circulation in the middle and upper troposphere. A blocking surface high to the north usually isolates the low from potential sources of cold air. The upper-level low may form simultaneously with a surface occlusion of a frontal wave at low latitudes. Alternatively, cyclogenesis may occur in the midlevels and then extend down to the surface. Kona lows have erratic tracks and can propagate westward for long distances. Simpson noted that the strongest surface winds occur to the east and northeast of the low center, and the maximum rainfall occurs on the southeast side of the low.

Ramage (1962) suggested the kona low's circulation is strongest between 400 and 600 mb. Convergent warm, moist air rises up from the south on the southeast side of the low; and cold, dry air from the north subsides on the western side of the low in a thermally direct system. Ramage had access to data resources similar to those of Simpson, with the addition of the first *Television and Infrared Observational Satellite* (*TIROS-1*) images.

Numerical weather prediction models generally perform poorly on kona low development and track. The models have difficulty simulating the mesoscale structures of these systems, a circumstance that is exacerbated by a lack of data over the central Pacific Ocean and insufficient model resolution (Businger et al. 1998). The central pressure forecasts for the kona low of February 1997 from the aviation run of the National Centers for Environmental Prediction (NCEP) Global Spectral Model (AVN) show a pattern of early deepening followed by rapid filling (Fig. 2a). Each simulated storm deepens significantly less than observed and dissipates too rapidly (Fig. 2a). The AVN run for 0000 UTC February 23 places the initial low ~700 km away from the observed position and brings it no closer than ~500 km by the end of the model run (Fig. 2b). The later AVN runs produce more realistic tracks of the low but the average position error is still 300 km.

The purpose of this study is to investigate the synoptic-scale evolution of the kona low. This includes upper-level kinematics and thermodynamics, atmospheric stability, and vorticity tendencies associated with the low. Restricted datasets limited early studies done by Ramage and Simpson. The current study employs all available observational data and data from the NCEP–National Center of Atmospheric Research (NCAR) reanalysis project (Kalnay et al. 1996), discussed further

in section 2. This study focuses primarily on the synoptic spatial scale to be consistent with the resolution of the reanalysis dataset (2.5°). The relationship between the synoptic-scale dynamics and the areas of convection is investigated with the aid of *Geostationary Operational Environmental Satellite-9 GOES-9* satellite data. In the absence of radar data or in situ aircraft data, a detailed mesoscale investigation is beyond the scope of this study.

A four-times-daily analysis was conducted over a period of 4 days. Five time periods in the prolonged life cycle of the kona low are selected to illustrate salient aspects of the dynamic evolution of the storm (Fig. 1a). For reference and clarity the five stages are named (i) incipient (1800 UTC 23 Feb), (ii) intensifying (1200 UTC 24 Feb), (iii) mature (1200 UTC 25 Feb), (iv) weakening (1200 UTC 26 Feb), and (v) dissipating (1200 UTC 27 Feb). The incipient stage is the time when the first closed isobar appears at the surface. The surface low deepens at its maximum rate during the intensifying stage. The time of lowest surface pressure occurs during the mature stage. The weakening and dissipating stages, both with similar rates of filling, depict the low's decline.

2. Data resources and methods

Sea level pressure charts were subjectively analyzed every 6 h incorporating station observations, ship reports, and buoy data. The National Climatic Data Center supplied ship and buoy reports that were not available in real time. All reports include some or all of the following: temperature, dewpoint temperature, wind direction, wind speed, and pressure. In addition, long-line fishing boat records that include ship position, wind direction, and wind speed for the Hawaiian waters were obtained from archives at the National Marine Fisheries Service Laboratory in Honolulu and used to further improve the accuracy of the sea level pressure analyses.

Visible, infrared, and water vapor images from *GOES-9* are available every hour for most of the observational period (Figs. 3 and 4). Satellite analyses of the low-level cloud patterns aided in locating the center of the surface low. Areas of cold cloud inferred from IR satellite data (Fig. 4) are used as an overlay on many of the analyses presented in section 3 to show the relationship of the analyzed or derived fields and the extent of cold clouds tops (e.g., Fig. 5). The threshold temperature (-40°C) for the overlays was chosen on the basis of the tropopause temperatures observed at Hilo from rawinsonde data during the event. At the time of convection over the island of Hawaii, the tropopause was located near 200 mb with a temperature of ~ -45°C. Cloud tops reaching the tropopause do not necessarily equate to deep convection but infer a history of ascent, perhaps within convective towers. Deep convection can, however, be inferred from small, distinct cold-top features with sharp lateral temperature gradients in the IR satellite imagery (Fig. 4) (Kidder and Vonder Haar 1995).

The NCEP–NCAR reanalysis dataset (hereafter reanalysis dataset) provides a special opportunity to examine the synoptic-scale dynamic evolution of the kona low, particularly above the surface. The NCEP–NCAR reanalysis project (Kalnay et al. 1996) uses an analysis/forecast system to perform data assimilation on NCEP Global Telecommunications System (GTS) data. NCEP GTS includes data from the global rawinsonde network, commercial aircraft (Fleming 1996), the Comprehensive Ocean–Atmosphere Data Set, surface marine data, surface land synoptic data, TIROS-N Operational Vertical Sounder data, Special Sensing Microwave/Imager (SSM/I) data, and satellite cloud drift winds. Reanalysis was completed using a T62 global spectral model (2.5° resolution; see Fig. 6) with 28 vertical levels including parameterizations of all major physical processes. Two atmospheric levels in the reanalysis dataset, the 250-mb level and sea level, benefit from a concentration of in situ and remotely sensed data over the central Pacific Ocean. Data aloft are acquired from in situ measurements from aircraft, rawinsondes, and satellite data. At the surface, data are gathered from standard observations, ships of opportunity, buoys, and satellite derived quantities (e.g., winds, SST).

To assess the quality of the reanalysis data, comparisons were made between objective surface analyses of the reanalysis data and subjective surface analyses. The position error for each analysis shows a diminishing distance between positions from the incipient stage to the intensifying stage and then a difference of 220 km or less for the remaining stages (Fig. 1a). The reanalysis analyzed track provides a good fit to the observed storm track and is within the resolution of the reanalysis, $\sim$275 km at this latitude. This level of agreement is valid for all stages except the incipient stage where the track position differs by 330 km. This error may be attributed to the fact that there were two weak circulation centers during this early growth stage. The observations support lower pressure in the enhanced analyses, but the trend in the reanalysis data follows the observed minimum sea level pressure (MSLP) well (Fig. 1b). The mean difference between observed and reanalysis MSLP during the life cycle of the low was 2 mb. This bias can largely be attributed to the coarse resolution of the reanalysis data and additional smoothing during the objective analysis. Additionally, reanalysis data and Hilo rawinsonde data were compared. Upper-air winds from the Hilo rawinsondes match consistently with the derived reanalysis winds throughout the period. Objective analyses based on the reanalysis dataset are used to investigate the evolution of synoptic-scale features associated with the kona low.

3. Results

The kona low investigated in this paper deepened downward from the upper troposphere. The analyses

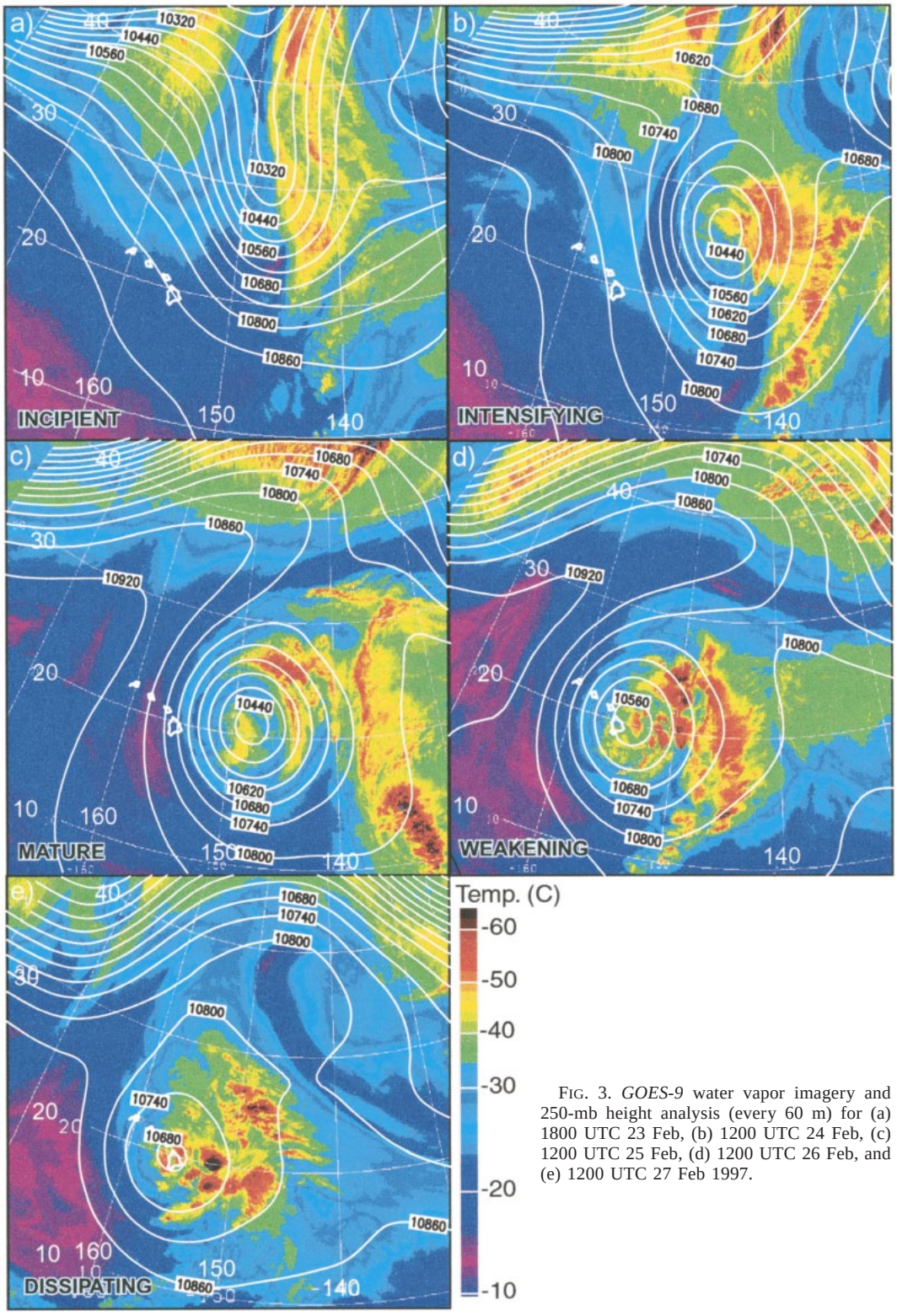

FIG. 3. *GOES-9* water vapor imagery and 250-mb height analysis (every 60 m) for (a) 1800 UTC 23 Feb, (b) 1200 UTC 24 Feb, (c) 1200 UTC 25 Feb, (d) 1200 UTC 26 Feb, and (e) 1200 UTC 27 Feb 1997.

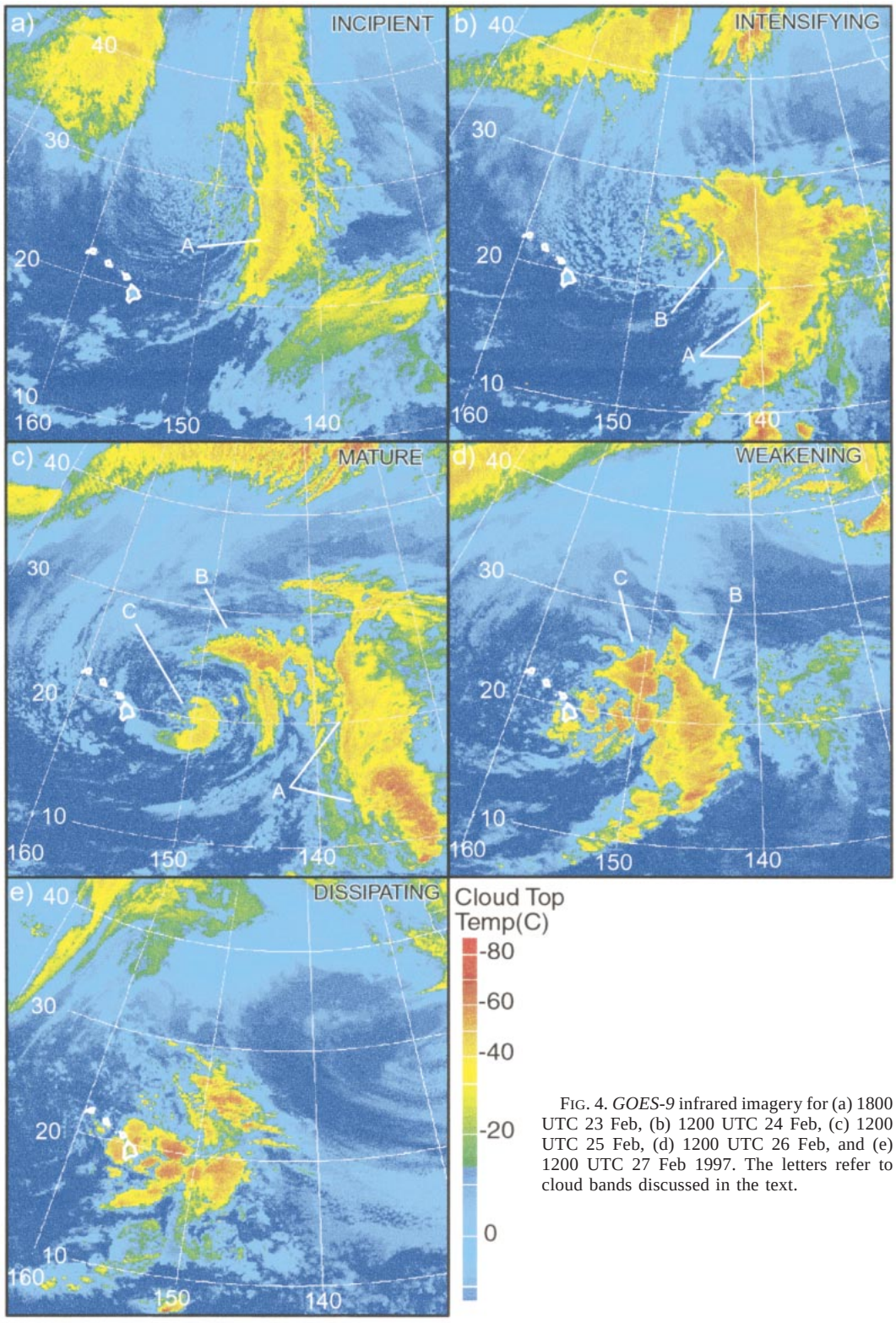

FIG. 4. *GOES-9* infrared imagery for (a) 1800 UTC 23 Feb, (b) 1200 UTC 24 Feb, (c) 1200 UTC 25 Feb, (d) 1200 UTC 26 Feb, and (e) 1200 UTC 27 Feb 1997. The letters refer to cloud bands discussed in the text.

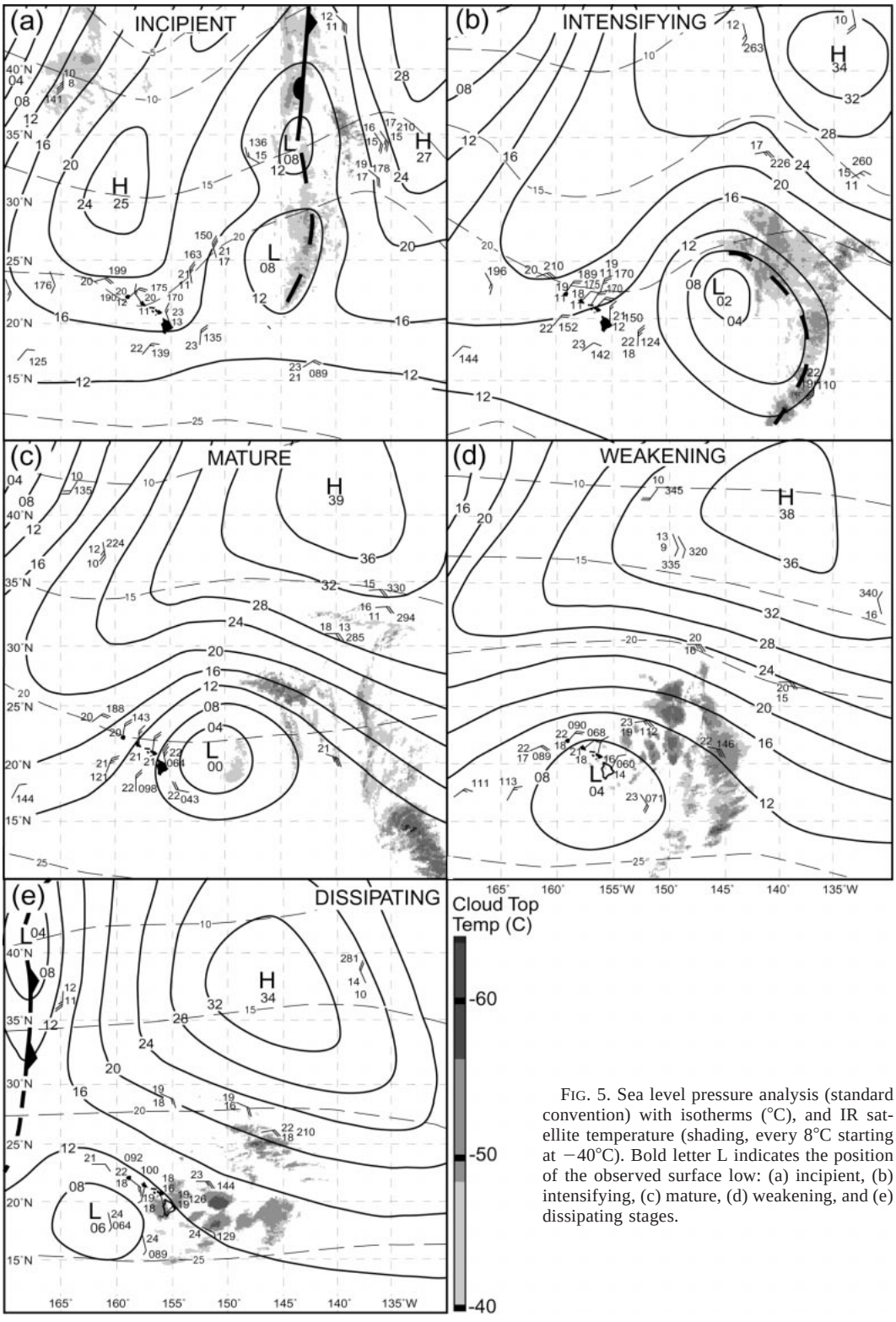

FIG. 5. Sea level pressure analysis (standard convention) with isotherms (°C), and IR satellite temperature (shading, every 8°C starting at −40°C). Bold letter L indicates the position of the observed surface low: (a) incipient, (b) intensifying, (c) mature, (d) weakening, and (e) dissipating stages.

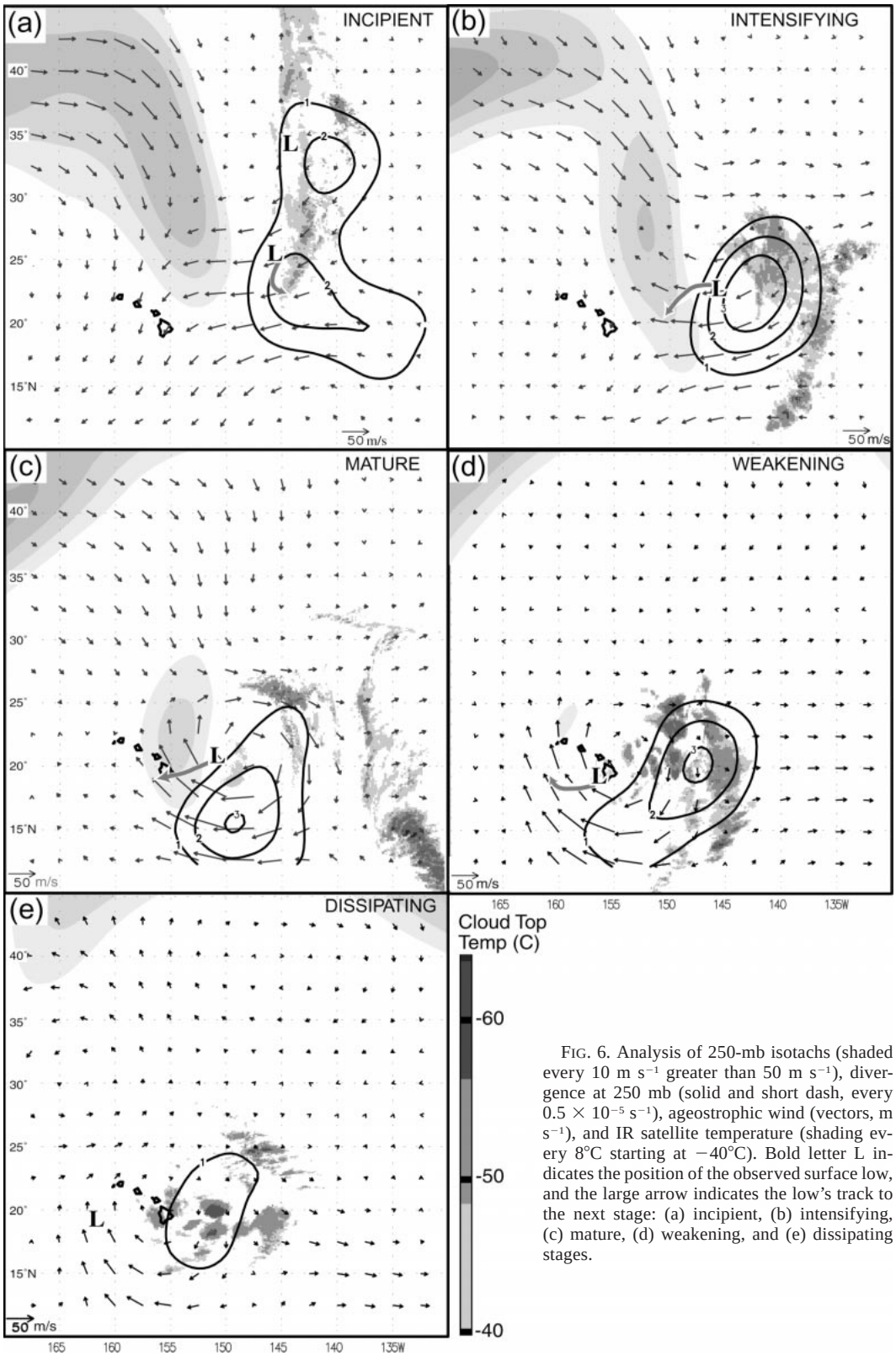

FIG. 6. Analysis of 250-mb isotachs (shaded every 10 m s^{-1} greater than 50 m s^{-1}), divergence at 250 mb (solid and short dash, every 0.5×10^{-5} s^{-1}), ageostrophic wind (vectors, m s^{-1}), and IR satellite temperature (shading every 8°C starting at −40°C). Bold letter L indicates the position of the observed surface low, and the large arrow indicates the low's track to the next stage: (a) incipient, (b) intensifying, (c) mature, (d) weakening, and (e) dissipating stages.

presented in this section emphasize upper-level and surface development, coinciding with two levels in the reanalysis that benefit from a concentration of in situ and remotely sensed data.

a. Satellite analysis

GOES-9 water vapor data are useful for depicting the evolution of the kona low's development in the upper troposphere (Weldon and Holmes 1991). Cloudless regions show emissions from water vapor located between 600 and 300 mb (Morel et al. 1978). In cloudy regions, strong water vapor emissions (dark red to light red regions in Fig. 3) likely include contamination from high cirrus or cumulonimbus clouds that reach the upper troposphere (e.g., Kidder and Vonder Haar 1995).

During the incipient stage a long cloud band stretches along ~142°W and reaches as far south as ~20°N coinciding with a stalled trough at the surface (Figs. 3a and 5a). The drier air (light blue to magenta regions) that extends parallel and west of the moist band is associated with a jet stream north of the islands (Figs. 3a and 6a). At this time the infrared satellite imagery shows cold cloud tops along the stalled surface trough with evidence of deep convection occurring within cloud band A along the southern portion of the trough (Figs. 3a and 4a). Early development of the kona low was observed as an S-shaped bulge along the southern half of the moist band that became more prominent during the next 12 h (not shown).

Development continues and a comma head emerges by the intensifying stage with a trailing cloud band extending to the south (Figs. 3b and 4b). The dry slot aloft maintains its position to the west of the band. Convective cells can be inferred from sharp temperature gradients along the southern portion of the outer cloud band A and within an inner cloud band B closest to the center of circulation (Figs. 3b and 4b). The distance between band A and band B is ~600 km.

By the mature stage, there are two synoptic-scale cloud bands and a third band emerging just east of the circulation center, with evidence of dry air between each band (Figs. 3c and 4c). Satellite image analysis suggests the presence of convective cells within bands C and B. Whereas a relative lack of temperature variations suggests that high cirrus and altostratus clouds dominate cloud band A, which is propagating eastward away from the circulation center. The distance between bands A and B has remained ~600 km and the distance between bands B and C is ~500 km.

By the weakening stage, the outer cloud band maintains its integrity and the innermost features of the kona low maintain an organized structure, but the banded organization of the clouds and moisture becomes less evident (Figs. 3d and 4d). During the weakening stage only two large-scale cloud bands are visible (Fig. 4d). The inner cloud band C contains scattered convective cells and the outer cloud band B contains some convective cells but appears to contain mostly cirrus and altostratus clouds. The distance between bands B and C has remained ~500 km.

The water vapor image of the dissipating stage reveals deep moisture over Maui and the Big Island near the center of the circulation aloft (Figs. 3e and 4e). Isolated convective cells over the Big Island and Maui produce reports of hail and heavy rains, and satellite imagery shows evidence of isolated areas of deep convection surrounding the Big Island. The outer band has dissipated and the large-scale cloud structure has lost most of its banded organization by this time.

In general, the synoptic-scale cloud bands tracked eastward away from the surface low and slowly dissipated. Their average life span was ~60 h. Smaller-scale convective features, exhibiting wavelengths about ~100 km, are also evident in satellite imagery during the life cycle of the kona low. These features, visible between the large-scale bands, are most apparent in Fig. 4c and are discussed further in section 5.

b. Upper-tropospheric dynamics, surface development, and stability

The effect of upper-tropospheric dynamics on stability and cyclogenesis is examined in this section. In part, quasigeostrophic diagnostics will be applied to help understand the evolution of the kona low (e.g., Holton 1992). Ageostrophic horizontal winds and quasigeostrophic vertical velocity are those motions required to keep geostrophic advection from producing large disruptions in the hydrostatic and geostrophic balance (Durran and Snellman 1987). Implicit in quasigeostrophic analysis are the assumptions that the large-scale flow is adiabatic and tends toward thermal wind balance, with ageostrophic motions an order of magnitude weaker than the geostrophic wind. Therefore, the results of this analysis must be interpreted with caution in regions of deep convection and highly curved flow associated with the kona low. These limitations will be discussed further in section 5.

Prior to the kona low's development, an extratropical cyclone had swept across the central North Pacific with a trailing cold front, oriented northeast to southwest, passing over the Hawaiian Islands and then continuing to the east. As the extratropical cyclone approached the northwest coast of the United States, cyclogenesis occurred on 23 February 1997 along the now-stalled trough northeast of Hawaii (Fig. 5a). As mentioned at the outset of this section, the kona low developed downward from the upper troposphere. The 250-mb wind pattern for the incipient stage shows a high-amplitude trough along 148°W longitude, with a jet streak >70 m s^{-1} along the west flank of the trough (Figs. 3a and 6a).

The relationship of the leftward-directed ageostrophic wind in the jet exit region and the 250-mb divergence field is apparent in Fig. 6a. A band of cold clouds is found along the axis of greatest divergence aloft and

two surface lows along the stalled surface trough are found just west of two areas of greatest upper-level divergence (Figs. 5a and 6a). Enhanced curvature in the vicinity of the sharp trough contributes to the vorticity (e.g., Fig. 7a), with enhanced positive vorticity advection (PVA) east of the trough axis (not shown) also contributing to upward motion over the region of developing cloud bands.

The southernmost surface low develops dramatically during the next 18 h (intensifying stage), under the region of divergence aloft associated with the left exit region of the jet streak and the influence of enhanced PVA (Figs. 5b, 6b, and 8a). Ageostrophic flow is greatest at this time and a large area of cold cloud tops is located within the area of enhanced divergence aloft (Fig 6b). A surface ridge initially located to the east of the surface low builds westward placing a ridge to the north and west of the low. Thus, separating the low from the westerlies located farther north by the intensifying stage (Fig. 5b). The surface pressure gradient between the building anticyclone and the deepening low strengthens substantially by 1800 UTC 24 February (not shown) advecting cool, dry air over the island chain from the north.

Further deepening of the surface low to 1000 mb and strengthening of the ridge (1039 mb) to the north ensures strong easterly flow on the low's north flank by the mature stage (Fig. 5c). Surface isotherms are oriented zonally at this time, reflecting a lack of frontogenesis at the surface, likely because of the frontolytic role of surface fluxes and subsidence of the air surrounding the low. Aloft, the southern end of the trough separates from the progressive large-scale trough to the north, resulting in a cold-core circulation that is secluded from the upper-level westerlies (Figs. 3c and 6c). By this time, the maximum winds aloft have weakened slightly (60 m s^{-1}), but remain located on the western side of the circulation. The maximum divergence has shifted to the southwest by the mature stage (Fig. 6c). The two outer cloud bands have moved eastward away from the center of maximum divergence, and a new convective cloud band is forming just north of the divergence center.

The kona low passes from east to west over the Big Island and unstable air from the Tropics is advected over the eastern section of the island chain during the weakening and dissipating stages of the storm (Figs. 5d and 5e). Thunderstorms and accompanying heavy rains occurred on the southeast coasts of the Big Island and Maui on 27 and 28 February. The weakening stages reveal a marked decrease in the maximum wind speeds aloft, but their location remains on the west flank of the closed low, as it has throughout the kona low's life cycle (Figs. 3d and 3e and 6d and 6e). By the dissipating stage the surface low has drifted more than 500 km west of the upper-level circulation center. New convection under the divergence area is evident during the weakening stage, whereas the older cloud bands have weakened and become more stratiform in character as they propagate eastward (Fig. 6d). The dissipating stage is characterized by decreasing values of divergence and vorticity and diminishing areas of cold cloud (Fig. 6e). Following the dissipating stage the surface trough and trough aloft eventually merged with a system approaching from the northwest (Figs. 3e and 5e).

Assuming inviscid flow, the principle of the conservation of potential vorticity allows the adiabatic transport of stratospheric air to be tracked. An increase in cyclonic vorticity occurs as stratospheric air descends into the troposphere. The increase in vorticity is due to the decrease in static stability that accompanies vortex tube stretching (Reed and Danielson 1959; Holton 1992). Reed and Danielson (1959) and Shapiro (1976) document stratospheric air entering the troposphere with threshold potential vorticity values $>10 \times 10^{-5}$ K mb^{-1} s^{-1}.

The incipient stage is characterized by a reservoir of high potential vorticity ($>20 \times 10^{-5}$ K mb^{-1} s^{-1}) aligned along the axis of the high-amplitude trough (Fig. 7a). Positive θ_e advection ($10–20 \times 10^{-5}$ K s^{-1}) is located near the surface pressure trough along the leading edge of the high potential vorticity, consistent with a low-level response to the upper-level PV anomaly (e.g., Hoskins et al. 1985). Low-level positive θ_e advection encompasses both large-scale cloud bands during the intensifying stage, with the warm advection located beneath the leading edge of the stratospheric potential vorticity anomaly (Fig. 7b). The maximum potential vorticity values have diminished from 30 to 20×10^{-6} K mb^{-1} s^{-1} by the mature stage (Fig. 7c). The θ_e advection reaches its maximum (30×10^{-5} K s^{-1}) during this period, maintaining a position under the leading edge of the potential vorticity anomaly and encompassing the two cloud bands closest to the surface low. In the decaying stages the potential vorticity decreases to 15×10^{-6} K mb^{-1} s^{-1} (Fig. 7d), but substantial warm θ_e advection remains in the areas of cold cloud tops near the surface low. Potential vorticity diminishes further to 10×10^{-6} K mb^{-1} s^{-1} during the dissipating stage and the advection of θ_e from the south diminishes further, but it is sufficient to result in substantial deep convection near the Big Island (Fig. 7e).

Sustained ascent results in destabilization of the lapse rate and cyclogenesis (e.g., Hess 1959; Durran and Snellman 1987). Trenberth (1978) developed an efficient way to visualize regions susceptible to synoptic-scale ascent in a single chart. He showed that quasi-geostrophic vertical motions occur in regions where there is advection of vorticity by the thermal wind. The 500-mb vorticity maximum is located west of the 700–250-mb thickness trough for all stages (Fig. 8 shows intensifying and weakening stages), consistent with the evolution of the potential vorticity anomaly in Fig. 7. This configuration places enhanced PVA over the surface low and extends PVA in an arc to the west, south and east of the surface low. PVA to the west of the surface low supports the westward propagation of the

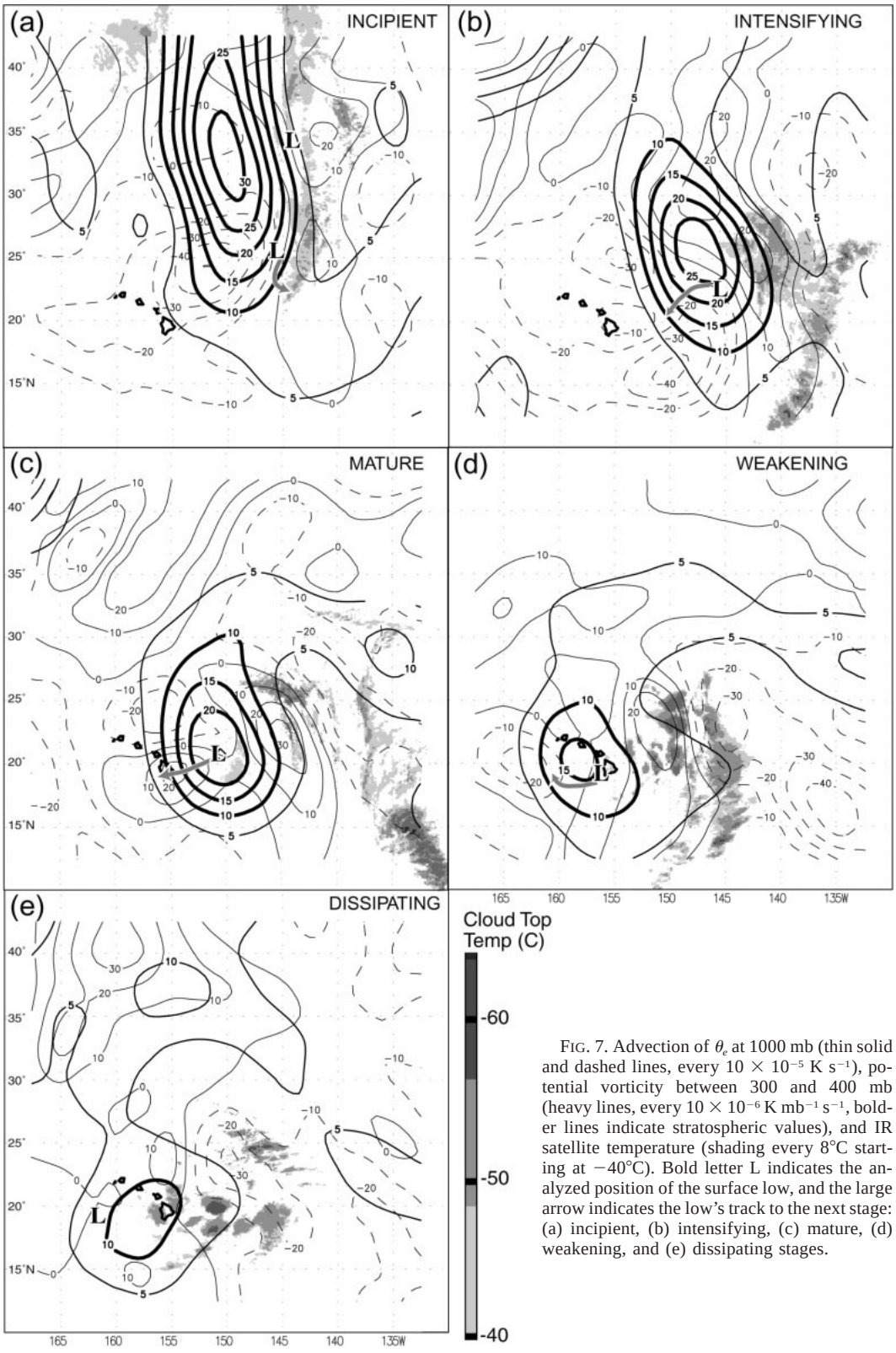

FIG. 7. Advection of θ_e at 1000 mb (thin solid and dashed lines, every 10×10^{-5} K s^{-1}), potential vorticity between 300 and 400 mb (heavy lines, every 10×10^{-6} K mb^{-1} s^{-1}, bolder lines indicate stratospheric values), and IR satellite temperature (shading every 8°C starting at −40°C). Bold letter L indicates the analyzed position of the surface low, and the large arrow indicates the low's track to the next stage: (a) incipient, (b) intensifying, (c) mature, (d) weakening, and (e) dissipating stages.

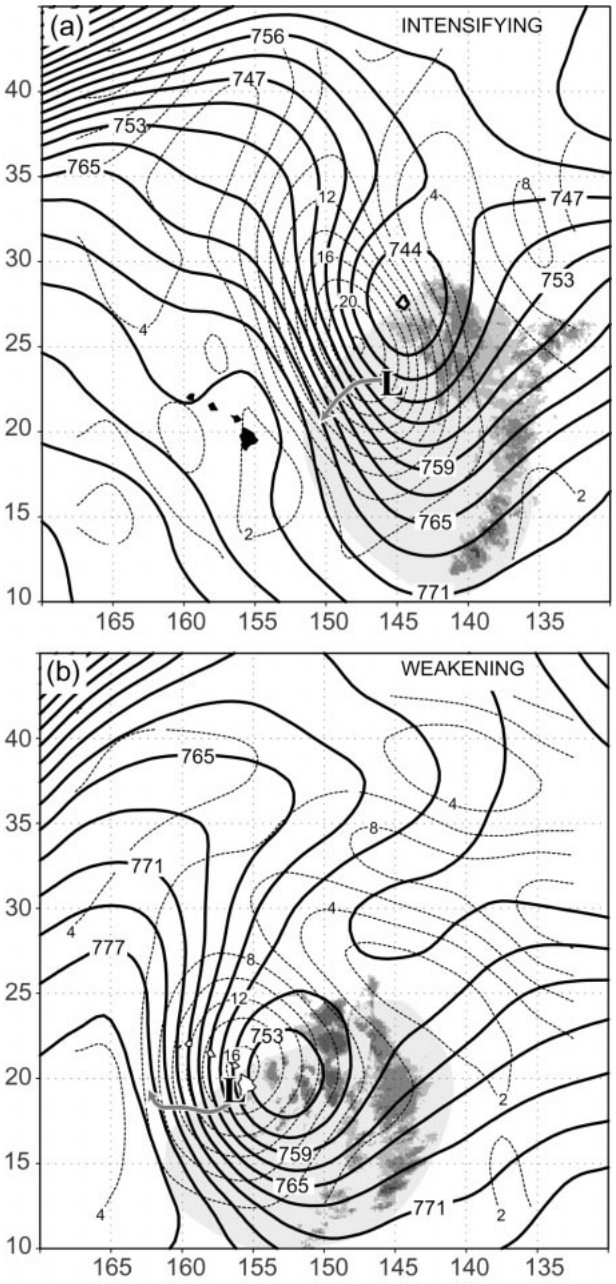

FIG. 8. Absolute vorticity at 500 mb (dash line, every 2×10^{-5} s^{-1}), 700–250-mb thickness (solid line, every 30 m), dark shading indicates area of cold cloud tops (IR temperature < -40°C), and area of positive vorticity advection at 500 mb (light shading). Bold letter L indicates the analyzed position of the surface low, and the arrow indicates the low's track to the next stage: (a) intensifying and (b) weakening stage.

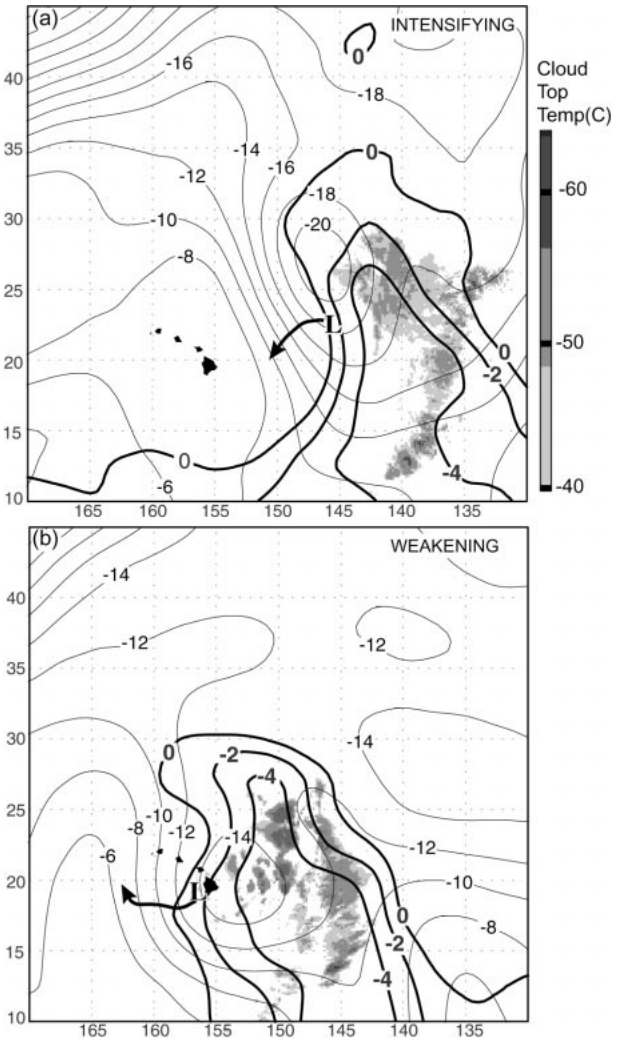

FIG. 9. Best lifted index (bold lines $\leq$0°C), 500-mb temperature (thin lines, °C), and IR satellite temperature (shading every -8°C starting at -40°C). Bold letter L indicates the analyzed position of the surface low, and the large arrow indicates the low's track to the next stage: (a) intensifying stage and (b) weakening stage.

kona low. PVA is enhanced over the region of greatest moisture advection to the east and southeast of the surface low (Figs. 7 and 8), aiding the development of new convection to the west of older convective rainbands. During the intensifying stage (Fig. 8a) the area of PVA includes a developing convective cloud band (labeled B in Fig. 4b), as well as the current and future position of the surface low to the west. During the weakening stage PVA encompasses the surface low and the area of convection to the southeast of the low (Fig. 8b).

The best-lifted index (BLI) was developed to diagnose areas susceptible to deep convection (Fujita et al. 1970). The lowest value of the lifted index (Galway 1956) obtained from an average parcel (mean mixing ratio and mean virtual temperature) in a layer defines the BLI. The layers being lifted in this case are between the pressure heights of 1000, 925, 850, and 700 mb. As with the lifted index, a negative temperature difference (BLI < 0) implies positive buoyancy and upward accelerations of an air parcel reaching this height. Analysis shows that areas with negative values of BLI are located to the east of the surface low during all stages (Fig. 9).

Moreover, the areas of negative BLI consistently correlate with convective areas for all stages. The cold cloud tops remain along the leading edge of the pool of coldest air at 500 mb during the first three stages (e.g., Fig. 9a). In the weakening and dissipating stages the cold cloud tops shift closer to the center of the coldest air aloft (Fig. 9b). The greatest instability was diagnosed during the mature stage with a BLI value of −8°C (not shown) while the remaining stages maintain a value of at least −4°C. The unstable areas (BLI < 0) correspond to the areas of low-level warm advection of θ_e (Figs. 7 and 9).

c. Vertical cross sections and profiles

East–west cross sections are presented here to document the synoptic structure associated with the kona low during the intensifying and weakening stages (Fig. 10). The cross sections, analyzed from the reanalysis dataset, are centered above the surface low and extend 10° longitude in each direction. Height and temperature anomalies were calculated by subtracting an average environmental value from the area bounded by 10°–35°N and 170°–130°W from the grid values for each stage.

Cross sections of height and temperature anomalies (H' and T') indicate a cold-core system with greatest H' occurring at 250 mb. The axis of the T' intersects the position of the surface low at ~450 mb during the intensifying stage (Fig. 10a). Strong T' lie within the axis (−6° to −10°C) from 850 to 250 mb. The T' structure on the east side of the surface low is conducive to convection during the intensifying stage, showing anomalous warm temperatures at the surface and anomalous cold temperatures aloft. The western side of the low has cold T' near the surface and warm T' aloft creating a stable atmosphere for all stages. The intensifying stage has the largest cold cloud-top area and the largest T' difference (−10°C) with respect to height. The weakening stage maintains an anomaly of −6°C (Fig. 10b) while the dissipating stage is characterized by smaller cold T' (−2°C) (not shown). Generally, the coldest T' occur within an elongated axis between 250 and 850 mb.

The largest H' propagate from the west to east relative to the surface low. The maximum anomaly during the intensifying stage is located west (~120 km) of the surface low at 250 mb (Fig. 10a). The H' have reached the surface at this time and maintain a presence there for the remainder of the life span. The maximum H' propagates to the east of the surface low (~440 km) by the mature stage (not shown) and moves farther east through the weakening (~600 km) (Fig. 10b) and dissipating stages (~950 km).

Vorticity and divergence profiles were calculated above the storm center to give insight into cyclogenesis and vertical motion, respectively. The vorticity, divergence, and vorticity tendency terms are calculated using finite differencing and are averaged over a ~275 km radial column centered on the surface low. The incipient, intensifying, and weakening stages are characterized by increasing vorticity with height from the surface to 250 mb and then rapidly decreasing vorticity with height above 250 mb (Fig. 11a). Maximum vorticity values are found in the upper troposphere for all stages except the dissipating stage, with the largest vorticity value overall found in the intensifying stage. The mature stage has the largest vorticity of any stage below 400 mb. It shows a maximum at 500 mb and rapidly decreasing vorticity above 300 mb.

The vorticity profiles are well behaved at most levels with each profile through the mature stage having more

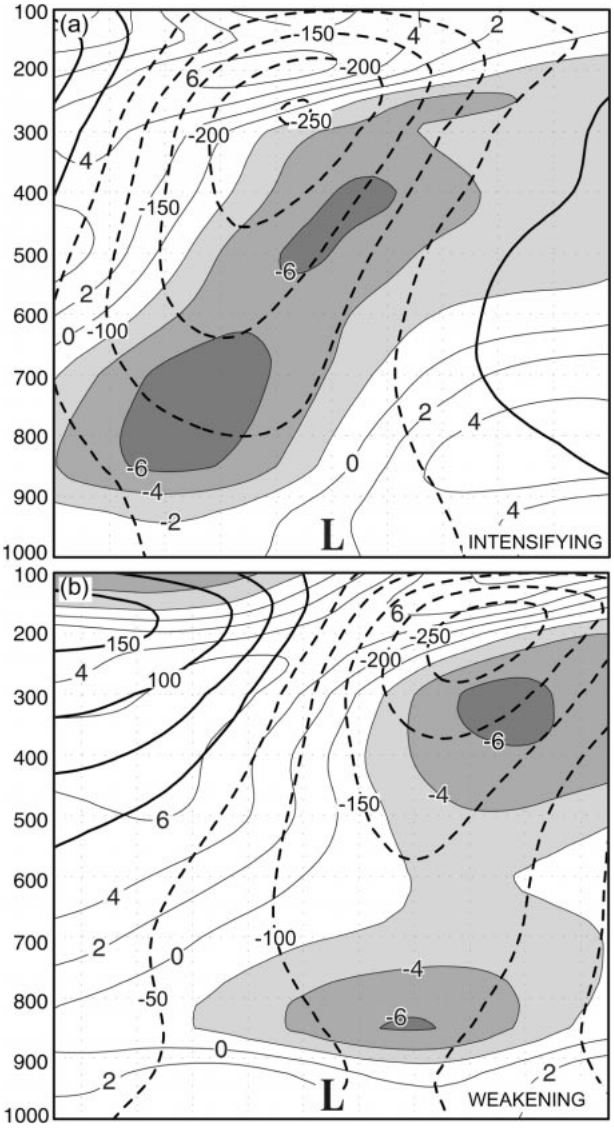

FIG. 10. Cross section of height anomalies (bold dashed lines, m) and temperature anomalies (light lines and shaded regions, °C): (a) intensifying and (b) weakening stages. Bold letter L indicates the reanalysis position of the surface low.

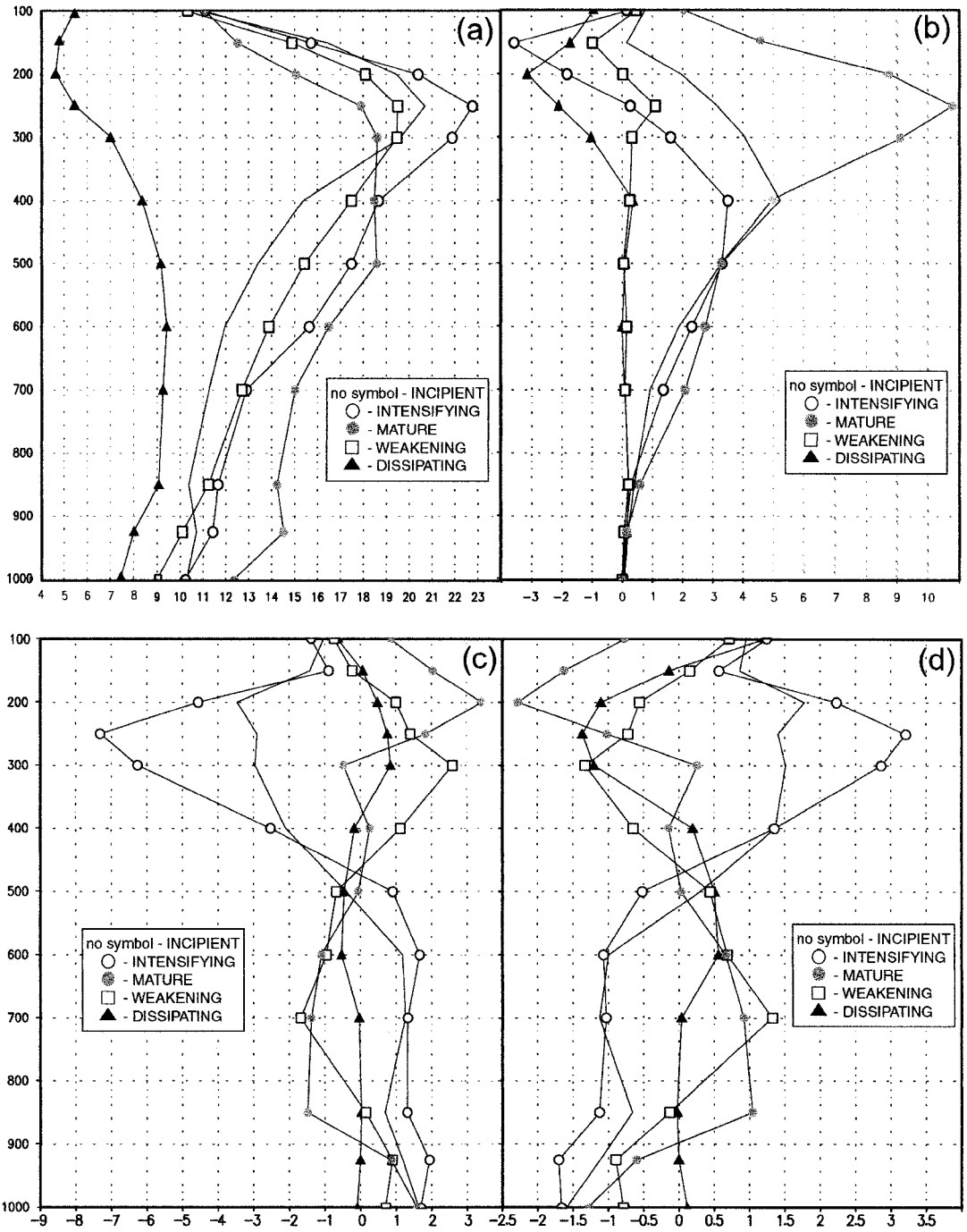

FIG. 11. Vertical profiles of (a) vorticity (10^{-5} s^{-1}), (b) vorticity due to horizontal vorticity advection (10^{-9} s^{-2}), (c) vorticity due to divergence (10^{-9} s^{-2}), and (d) divergence (10^{-5} s^{-1}) for incipient (no symbol), intensifying (open circle), mature (closed circle), weakening (open square), and dissipating (closed triangle) stages.

vorticity than the last and then showing diminishing vorticity with time during the last two stages. As the surface low moves westward relative to the upper-level low, a gradual process of decoupling starts at about the time of the mature stage. The significant reduction in vorticity from weakening to dissipating stage reflects in part the impact of this decoupling (Fig. 11a). However, a computational effect may also contribute to the reduced vorticity by the dissipating stage as the distance between the surface and the upper-level circulation centers increases to a scale approaching that of the radial distance used in the calculations. Therefore, the results

for this last stage should be interpreted with some caution.

The vorticity tendency equation is applied to the radial column of air above the surface low:

$$\partial\zeta/\partial t = -\mathbf{V}_H \cdot \boldsymbol{\nabla}(\zeta + f) - \omega(\partial\zeta/\partial p) - \boldsymbol{\nabla} \cdot \mathbf{V}_H(\zeta + f) + (\partial u/\partial p)(\partial\omega/\partial y) - (\partial v/\partial p)(\partial\omega/\partial y). \quad (1)$$

The terms on the right side of Eq. (1) represent horizontal vorticity advection, vertical advection in pressure coordinates, vorticity generated by divergence, and the last two terms represent the vorticity generation by tilting of vortex tubes. The vertical advection and tilting terms scale out of the equation for synoptic-scale motions and the two significant terms left are the horizontal advection and divergence terms. The resulting equation is similar to the quasigeostrophic vorticity tendency equation, except for the substitution of the geostrophic wind in the latter form (Bluestein 1992, p. 326).

Horizontal advection of vorticity dominates the middle and upper troposphere during the growth stages and provides the largest contribution to the vorticity tendency during the mature stage (Fig. 11b). The later stages are characterized by little contribution to the vorticity tendency except slight negative values aloft. Vorticity generated by divergence controls the lower-tropospheric cyclogenesis during the growth stages, while contributing large negative values in the upper troposphere (Fig. 11c). In the later stages the sign of this term reverses (except in the lowest levels); however, the positive and negative values are smaller.

Vertical profiles of divergence, averaged over a 275-km radius surrounding the storm centers, are shown for the five stages of the kona low in Fig. 11d. Convergence from the surface to 500 mb and divergence above 500 mb characterize the growth stages. The last three stages show weak convergence near the surface, divergence from 850 to 450 mb, and convergence aloft. There is a definite contrast between the two growth stages and the mature and decaying stages. The growth stages have a well-defined level of nondivergence while the mature and decaying stages show the divergence profile of a dissipating low pressure system.

d. Cyclone track

Kona lows have previously been shown to have erratic tracks (Simpson 1952) that are difficult to forecast (Fig. 2b; Businger et al. 1998). In the present case the vortex aloft propagated from east to west following the incipient stage (24 Feb at 1200 UTC; Fig. 1a). This behavior is common to cutoff lows that form over the central Pacific Ocean at the latitude of Hawaii. An isolated vortex with northerly flow on its western side will advect higher planetary vorticity southward; conversely on the circulation's eastern side southerly flow will advect lower planetary vorticity northward, resulting in a tendency for net westward propagation of the circulation

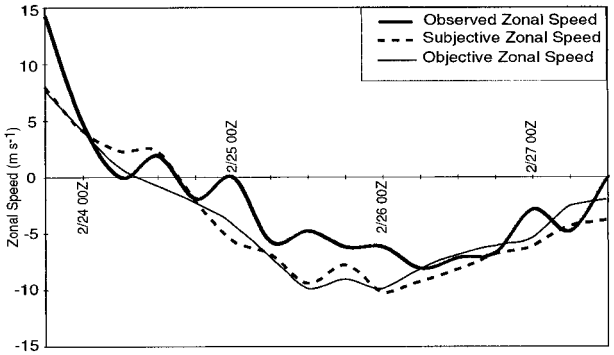

FIG. 12. Observed zonal speed (heavy solid line). Zonal phase speed estimated using a subjective analysis of the geostrophic wind (heavy dashed line). Zonal phase speed estimated using a 20° distance north and south of the low to calculate the geostrophic wind (thin solid line). See the text for details.

(Hoskins et al. 1985). Wu and Wang (2000) show that tropical cyclones move to the region where the azimuthal wavenumber one component of the potential vorticity tendency reaches a maximum. The closed low aloft in the case of the kona low can be thought of as a superposition of a number of Rossby waves of differing wavelengths. If the propagation of the circulation is dominated by a few waves with roughly similar spatial scales, it may be possible to estimate the propagation of the low by applying Rossby wave theory (e.g., Rossby et al. 1939; Durran 1988). In particular, a Rossby wave dispersion relationship [Eq. (2)] can be applied to a wave whose scale matches that of the kona low circulation near the level of nondivergence (Fig. 11d):

$$C_x = U - \beta/(k^2 + l^2), \quad (2)$$

where C_x is the zonal wave propagation, U is the mean zonal wind speed at 500 mb, β is the variation of the Coriolis parameter with latitude, and k and l are the zonal and meridional wavenumbers, respectively. The zonal propagation speed of the kona low was calculated at 6-h intervals from 500-mb height analyses. Wavenumbers k and l are measured from zonal and meridional ridge axes on either side of the low. The value of U is calculated by subjectively locating the ridgeline to north of the circulation center and using that distance to the north and south of the low to calculate the geostrophic wind (Fig. 12).

Overall the Rossby wave dispersion relationship provides a reasonable estimate of the zonal motion of the kona low. The dispersion relationship predicts the eastward propagation of the low through the intensifying stage and then reverses course back to the west for the remainder of the life cycle. The zonal propagation is slightly overestimated during the mature stage ($\sim$3 m s^{-1}). The method is relatively insensitive to the approach used in calculating the geostrophic wind. The geostrophic wind was also estimated using a 40° latitude interval centered on the closed low. The results of this *objective* approach are close to that of the first (Fig. 12), with the

latter approach having the advantage of being easier to apply operationally.

4. Summary and conclusions

During the last week of February 1997 a kona low produced record winds, blizzard conditions, high surf, thunderstorms, and hail. The kona low affected primarily the eastern end of the Hawaiian Island chain, causing upward of $4 million in damage. The research presented in this paper focused on the synoptic-scale aspects of the evolution of the kona low. The analysis was undertaken at 6-h intervals during the life cycle of the kona low using data from operational sources and the NCEP–NCAR reanalysis project. Five stages of the kona low's evolution were chosen to illustrate significant aspects of the storm's life cycle in this paper. This study focuses primarily on the synoptic spatial scale to be consistent with the resolution of the reanalysis data (2.5°).

Dynamics associated with a north–south-oriented jet streak and enhanced vorticity advection aloft was the mechanism for genesis. The jet streak occurred on the trailing side of a developing upper-level trough. An enhanced pressure gradient on the western side of the upper-level low was maintained as the circulation propagated westward toward an upper-level ridge; thus enhanced winds remained on the western side of the vortex throughout the low's life cycle. A close relationship was found between the ageostrophic wind and the 250-mb divergence field. Analyses suggest that high potential vorticity values, indicative of the intrusion of stratospheric air into the upper troposphere, induced enhanced positive advection of equivalent potential temperature near the surface. Quasigeostrophic analysis showed enhanced vorticity to the west of the thickness trough, a configuration that maintained an area of positive vorticity advection to the west of the surface low and over new convection east and southeast of the surface low.

The 250-mb level exhibited the strongest absolute vorticity values and the greatest height anomalies, contrary to earlier investigations of kona lows that emphasized a 500-mb circulation. The greatest temperature anomalies occurred along a vertically tilted axis extending from 850 mb in the west to 250 mb in the east. During the growth stages the axis of the negative temperature anomalies intersected the vertical plane of the surface low in the midtroposphere, reducing the static stability. During the decaying stages the axis of temperature anomalies intersected the surface low near sea level, reflecting a more stable stratification as the surface and upper-level lows decoupled. At the surface the isotherms showed a lack of baroclinicity, consistent with the equalizing influence from surface fluxes over a subtropical ocean on the cool-air side of the storm circulation.

The vorticity tendency was dominated by advection of vorticity aloft and by generation of vorticity by divergence below 500 mb during the growth stages. A gradual spindown of vorticity at all levels characterized the decaying stages. Divergence profiles showed a well-defined level of nondivergence at 500 mb during the growth stages, with low-level convergence and upper-level divergence. Later stages were characterized by smaller values of convergence and divergence, and the level of nondivergence became indistinct.

Cloud bands with embedded convective cells characterized the early and mature stages of the kona low in satellite imagery. The cloud bands formed on the low's eastern side and slowly propagated eastward, eventually leaving the area of synoptic-scale ascent and losing their convective characteristics. Later in the life cycle, the cloud bands were less organized and convection appeared more isolated. The average life span of the three synoptic-scale cloud bands was ~60 h. It was shown that regions of deep convection, as inferred from satellite imagery, coincided with areas of low-level advection of warm, moist air as diagnosed by advection of θ_c. Regions of deep convection also matched areas where the value of the best-lifted index was less than zero. Whereas the rainbands associated with the kona low tracked eastward, the storm circulation tracked westward from the intensifying stage onward. The Rossby wave dispersion relationship was found to provide a good estimate of the zonal propagation speed of the kona low throughout its life cycle.

5. Discussion

Quasigeostrophic analysis was undertaken to diagnose the relationship of the large-scale flow and the evolution of the surface low and associated rainbands. This paper may be the first to apply quasigeostrophic diagnostics to subtropical cyclogenesis. As discussed in section 3, when the results are interpreted, assumptions implicit in the derivation of quasigeostrophic equations need to be considered (e.g., Durran and Snellman 1987). In particular, the impact of diabatic heating and advection of momentum under conditions of highly curved flow are not represented in the theory. Nevertheless, patterns of upper-level ageostrophic motion, divergence, and PVA in Figs. 6 and 8 portray a congruous relationship between the location of inferred vertical motion, surface cyclogenesis, and convective rainband formation. These results lend confidence to the appropriateness of the analysis despite a weaker Coriolis force associated with the subtropical latitude. The midlatitude origin of the jet streak linked to the cyclogenesis may help explain in part the applicability of a quasigeostrophic analysis in this case. Moreover, the observation that Rossby wave theory is consistent with the zonal propagation of the low supports the central role of large-scale dynamics in the evolution of the kona low in this case.

The kona low cyclogenesis in this study initially occurred in the upper troposphere (~250 mb level) and

then extended to the surface, with little evidence of sea level baroclinicity throughout its life cycle. This evolution is similar to the development documented in Businger et al. (1998). Surface cyclogenesis in the 1997 kona low occurred along a stalled trough similar to Simpson's (1952) description, but the driving force behind the 1997 kona low genesis was dynamics associated with a jet streak in the upper troposphere. Simpson also describes upper-level lows extending their circulation to the surface but had insufficient data to fully investigate the upper-level dynamics. The present results are in contrast to some of the findings of Ramage (1962). Ramage inferred that the strongest winds and largest pressure gradients occurred in the layer between 400 and 600 mb. However, he conceded that insufficient data were available to complete an upper-level composite.

Simpson (1952) mentions reports of kona lows that evolve into tropical storms. Bosart and Bartlo (1991) investigate Tropical Cyclone Diana (1984) with some similar characteristics to the 1997 kona low. Diana formed as a frontal wave cyclone off the coast of Florida. The subtropical cyclone went on to become a hurricane as the upper-level cyclone drifted southwestward and dissipated. In contrast the 1997 kona low remained cold core. The different outcomes may be due to the difference in the evolution of the vertical shear of the horizontal winds and/or the difference in sea surface temperatures. The waters in the Gulf Stream were above the empirical 26.5°C threshold for tropical cyclone formation, whereas the sea surface temperatures beneath the kona low averaged ~23°C, well below the threshold value. However, there are documented cases of tropical cyclone formation over colder water (e.g., Pelissier and Lawrence 1981) and hurricane-like storms that form over significantly colder water have been reported (e.g., Businger and Baik 1991). These developments feature colder than normal upper-level environments associated with troughs or cutoff lows similar to the present case.

Regions of convection associated with tropical upper-tropospheric troughs (TUTTs) have some similarities with kona lows, but their circulations are significantly weaker. TUTTs commonly form over the subtropical Pacific and Atlantic Oceans during the warm season (Sadler 1967; Kelley and Mock 1982). The TUTT cell circulation can be detected clearly in the water vapor channel. It has weak temperature and height anomalies aloft that do not usually extend to the lower troposphere. Generally, TUTT cells do not affect the wind field below the trade wind inversion, but they can enhance trade wind convection by reducing the temperature aloft.

The environmental conditions favorable for the development of polar lows and kona lows may seem very different at first glance. However, high vorticity and cold temperatures characterize the synoptic scale of both systems aloft. Therefore, it is interesting to compare the cloud bands in a kona low with those observed in polar lows (Businger and Reed 1989). The large-scale cloud bands (~500 km spacing) identified in the kona low are very similar to cloud bands in a polar low over the north Atlantic Ocean, associated with the advection of mesoscale vorticity maxima in the upper troposphere (Zick 1983). Unfortunately, the reanalysis dataset is unable to resolve such mesoscale features.

Businger and Walter (1988) found rainbands in a cold-core low with a mean wavelength of 60–75 km. Their analysis suggests conditional symmetric instability (CSI) and symmetric wave-CISK (convective instability of the second kind) as being the possible mechanisms for rainband formation and maintenance. Mesoscale model output suggests the potential for CSI in the vicinity of convective bands in a 1994 kona low (Businger et al. 1998). The average spacing between the large-scale cloud bands (500–600 km) found in the 1997 kona low was much larger than either CSI or symmetric wave-CISK predicts. However, the shorter-wavelength cloud bands (~100 km) observed in the 1997 kona low (Figs. 4c and 4d) are consistent with CSI theory. Without the aid of radar and in situ aircraft data, definitive interpretation of the causal mechanisms of the kona low's multiple rainbands remains the subject of future inquiry.

Ramage has commented that, ''old subtropical cyclones never die, they are only caught up by troughs in the polar westerlies.'' This observation proved accurate for the 1997 kona low, and raises the question of how kona lows are maintained following their deepening phase. Significant latent heating on the eastern half of kona lows and radiational cooling on their western half may provide a diabatic source of potential vorticity that helps maintain the storm circulation. The consistent underestimate of the magnitude of the deepening in the 1997 kona low in global model forecasts suggests improvements to the model guidance are needed from an operational perspective. Global model deficiency may be the result of a lack of data over the Pacific Ocean and/or due to a deficiency in model resolution that impacts the way in which convection is parameterized in the models. Application of mesoscale models with assimilation of satellite (e.g., Tropical Rainfall Measuring radar, SSM/I, scatterometer, IR and GOES-derived soundings) and sferics data from a Pacific lightning detection network (Alexander et al. 1999) could help resolve these shortcomings and is the subject of future research.

Kona-low conceptual model and applications to forecasting

The findings in this paper represent the results from a single case study. Nevertheless, insofar as the results are consistent with previous kona low developments, they can be used to forge a conceptual model that may help forecasters anticipate storm evolution and the development of weather hazards associated with future kona lows. Dynamic forcing associated with a north–south-oriented jet streak at 250 mb was identified as a

primary mechanism for storm genesis and intensification. The formation of such a jet streak can be anticipated using NWP model guidance. Once a jet streak has formed, its progress and development can be tracked in water vapor imagery. When the circulation aloft has fully separated from the westerlies to the north, deepening at the surface will cease. Negative best-lifted index values and areas of positive advection of equivalent potential temperature can be used to diagnose likely areas for development of deep convection. Damaging winds are generally concentrated on the northern half of the storm circulation, leading to marine and coastal hazards from enhanced swell and surf particularly when the kona low forms to the southeast of the observed location. However, historically in large kona lows, strong winds have also been observed on the southeastern side ahead of the surface trough (Haraguchi 1980). The potential for severe weather and flash flooding is greatest on the southeastern and eastern side of the surface low, particularly in bands of deep convection that tend to form closer to the center of circulation and cold air aloft. Prolonged heavy rainfall and flash flooding can be anticipated with slow moving kona low rainbands. The threat of severe weather and flash floods is most pronounced for lows that form over or just west of the site. In Hawaii and similar locations with substantial orography, the potential for terrain to significantly enhance the storm winds and rainfall needs to be taken into account.

The Rossby wave dispersion relationship provides reasonable estimates of the zonal speed of the kona low in this investigation. Although the robustness of this tool needs to be verified with future storms, comparisons between the theory and operational model output may help identify forecast discrepancies. Westward propagation is common in kona lows during some portion of their life cycles. The kona low in this investigation propagated westward during most of its life cycle, while associated rainbands propagated slowly eastward and new convection developed to the west of older bands. In the absence of accurate mesoscale numerical guidance, clearing in the wake of kona low rainbands can lead to premature predictions of improving weather that fail to verify for the westward moving lows.

Acknowledgments. The authors would like to thank Gary Barnes and Robert Farrel for many useful discussions and suggestions made during the course of this work. The authors are also grateful to John Locatelli, Richard Reed, Paul Jendrowski, and Kevin Kodama for their reviews of an early draft of the manuscript. Dale Durran provided feedback regarding interpretation of the Rossby wave analysis. The final manuscript benefited from many constructive comments provided by two anonymous reviewers. The NOAA–CIRES Climate Diagnostic Center in Boulder, Colorado, provided access to the reanalysis data used in this research (http://www.cdc.noaa.gov/). The UCAR COMET Outreach Program supported this research under Grants UCAR S97-86992 and S98-87020.

REFERENCES

Alexander, G. D., J. A. Weinman, V. M. Karyampudi, W. S. Olson, and A. C. Lee, 1999: The effect of assimilating rain rates derived from satellites and lightning on forecasts of the 1993 Superstorm. *Mon. Wea. Rev.,* **127,** 1433–1457.

Bluestein, H. B., 1992: *Synoptic-Dynamic Meteorology in Midlatitudes.* Vol. I, Oxford University Press, 430 pp.

Bosart, L. F., and J. A. Bartlo, 1991: Tropical storm formation in a baroclinic environment. *Mon. Wea. Rev.,* **119,** 1979–2013.

Businger, S., and B. Walter, 1988: Comma cloud development and associated rapid cyclogenesis over the Gulf of Alaska: A case study using aircraft and operational data. *Mon. Wea. Rev.,* **116,** 1105–1123.

——, and R. J. Reed, 1989: Cyclogenesis in cold air masses. *Wea. Forecasting,* **4,** 133–156.

——, and J.-J. Baik, 1991: An arctic hurricane over the Bering Sea. *Mon. Wea. Rev.,* **119,** 2293–2322.

——, T. Birchard Jr., K. Kodama, P. A. Jendrowski, and J. Wang, 1998: A bow echo and severe weather associated with a kona low in Hawaii. *Wea. Forecasting,* **13,** 576–591.

Durran, D. R., 1988: On a physical mechanism for Rossby wave propagation. *J. Atmos. Sci.,* **45,** 4020–4022.

——, and L. W. Snellman, 1987: The diagnosis of synoptic-scale vertical motion in an operational environment. *Wea. Forecasting,* **2,** 17–31.

Fleming, R. J., 1996: The use of commercial aircraft as platforms for environmental measurements. *Bull. Amer. Meteor. Soc.,* **77,** 2229–2242.

Fujita, T. T., D. L. Bradbury, and C. F. van Thullenar, 1970: Palm Sunday tornadoes of April 11, 1965. *Mon. Wea. Rev.,* **98,** 26–29.

Galway, J. G., 1956: The lifted index as a predictor of latent instability. *Bull. Amer. Meteor. Soc.,* **37,** 528–29.

Haraguchi, P., 1980: Storm of January 8–10, 1980. State of Hawaii Department of Land and Natural Resources, C83, 33 pp. [Available from State of Hawaii Department of Land and Natural Resources, P.O. Box 621, Honolulu, HI 96809.]

Hebert, P. H., and K. O. Poteat, 1975: A satellite classification technique for subtropical cyclones. NOAA Tech. Memo. NWS SR-83, 87 pp. [Available from Southern Region Headquarters, 819 Taylor St., Rm. 10A26, Ft. Worth, TX 76102.]

Hess, S. L., 1959: *Introduction to Theoretical Meteorology.* Holt, 362 pp.

Holton, J. R., 1992: *An Introduction to Dynamic Meteorology.* Academic Press, 511 pp.

Hoskins, B. J., M. E. McIntyre, and A. W. Robertson, 1985: On the use and significance of isentropic potential vorticity maps. *Quart. J. Roy. Meteor. Soc.,* **111,** 877–946.

Kalnay, E. M., and Coauthors, 1996: The NCEP/NCAR 40-Year Reanalysis Project. *Bull. Amer. Meteor. Soc.,* **77,** 437–471.

Kelley, W. E., and D. R. Mock, 1982: A diagnostic study of upper tropospheric cold lows over the western North Pacific. *Mon. Wea. Rev.,* **110,** 471–480.

Kidder, S. Q., and T. H. Vonder Haar, 1995: *Satellite Meteorology: An Introduction.* Academic Press, 466 pp.

Kodama, K. R., and G. M. Barnes, 1997: Heavy rain events over the south-facing slopes of Hawaii: Attendant conditions. *Wea. Forecasting,* **12,** 347–367.

Morel, P., M. Desbois, and G. Szewach, 1978: A new insight into the troposphere with the water vapor channel of Meteosat. *Bull. Amer. Meteor. Soc.,* **59,** 711–714.

NCDC, 1997: *Storm Data.* Vol. 39, No. 2, 146 pp.

Pelissier, J. M., and M. B. Lawrence, 1981: Atlantic hurricane season of 1980. *Mon. Wea. Rev.,* **109,** 1567–1582.

Ramage, C. S., 1962: The subtropical cyclone. *J. Geophys. Res.,* **67,** 1401–1411.

——, 1995: Forecasters guide to tropical meteorology, AWS TR 240 updated. AWS/TR-95/001, AWS, USAF, 392 pp. [Available from Headquarters AWS, Scott AFB, IL 62225.]

Reed, R. J., and E. F. Danielson, 1959: Fronts in the vicinity of the tropopause. *Arch. Meteor. Bioklimatol.,* **11A,** 1–17.

Rossby, C.-G., and Coauthors, 1939: Relation between variations in intensity of the zonal circulation of the atmosphere and the displacements of the semi-permanent center of action. *J. Mar. Res.,* 38–55.

Sadler, J. C., 1967: The tropical upper tropospheric trough as a secondary source of typhoons and a primary source of tradewind disturbances. Hawaii Institute of Geophysics Rep. 67-12, 103 pp. [Available from HIG, 2525 Correa Rd., Honolulu, HI 96822.]

Schroeder, T. A., 1977a: Meteorological analysis of an Oahu flood. *Mon. Wea. Rev.,* **105,** 458–468.

——, 1977b: Hawaiian waterspouts and tornadoes. *Mon. Wea. Rev.,* **105,** 1163–1170.

Shapiro, M. A., 1976: The role of turbulent heat flux in the generation of potential vorticity in the vicinity of upper-level jet stream systems. *Mon. Wea. Rev.,* **104,** 892–906.

Simpson, R. H., 1952: Evolution of the kona storm: A subtropical cyclone. *J. Meteor.,* **9,** 24–35.

Trenberth, K. E., 1978: On the interpretation of the diagnostic quasi-geostrophic omega equation. *Mon. Wea. Rev.,* **106,** 131–137.

Weldon, R. B., and S. J. Holmes, 1991: Water vapor imagery interpretation and applications to weather analysis and forecasting. NOAA Tech. Rep. NESDIS 57, 213 pp. [Available from NESDIS Headquarters, Route E/5011, Building FB41, 5200 Auth Rd., Suitland, MD 20746-4304.]

Wu, L., and B. Wang, 2000: A potential vorticity tendency diagnostic approach for tropical cyclone motion. *Mon. Wea. Rev.,* **128,** 1899–1911.

Zick, C., 1983: Method and results of an analysis of comma cloud developments by means of vorticity fields from upper tropospheric satellite wind data. *Meteor. Rundsch.,* **36,** 69–84.